Fabrication of Cerium Doped Nickel-Cobalt Ferrite by Co-Precipitation Method

Saira Yasmeen[1], H. M. Noor ul Huda Khan Asghar[1*], Zaheer Abbas Gilani[1], Muhammad Khalid[2]

[1] Department of Physics, Balochistan University of Information Technology, Engineering & Management Sciences, Quetta 87300, Pakistan
[2] Department of Physics, University of Karachi 24700, Pakistan

ARTICLE INFO

ABSTRACT

In the modern world researchers caught the attraction towards spinal ferrites. The current work is based on spinel ferrites having formula $Ni_{0.5}Co_{0.5}Ce_xFe_{2-x}O_4$ where (x = 0.0, 0.05, 0.1, 0.15, 0.2) Prepared by co-precipitation method. The confirmation of spinal ferrite structure was done through XRD analysis. The crystallite size was found to be in the range of 8 to 11 nm. Lattice perimeter is observe to obey the increasing trend due to replacement of larger ionic radii of cerium with smaller ionic radii of iron. Koop's phenomenological theory, Maxwell–Wagner interfacial polarization and Vegard's law is used to explain the behavior of lattice constant. The electrical properties of prepared ferrites were revealed by impedance analyzer. Various parameters like real and imaginary parts of dialectic constant, impedance and modulus was determined. In the frequency range of 1 to 3 GHz the detailed electrical inspection was done. During the electrode polarization the effect of grains on the increasing substitution of cerium was analyzed through real and imaginary parts of electrical modulus M' and M". In the frequency range of 3 GHz the value of M' is 2.1934×10^{-1} to 2.6581×10^{-1} and the value of M" is from 4.67×10^{-3} to 3.538×10^{-3}. AC conductivity spectra shows a non-Debye relaxation behavior and it dependents of conductivity on frequency. The observed dielectric constant, dialectic loss and tangent loss are found to be decreasing with the increase in frequency. The investigation shows that real and imaginary impedance Z' and Z" was found to be decreasing on lower frequencies and on higher frequencies all the curves merge with each other. The value of Z' and Z" at 3GHz frequency is in the range of 8.02×10^{-3} to 0.6073 and 3.7641 to 4.5617 respectively. Increase in frequency increases the AC conductivity. The applications of prepared nanoparticles are suggested in high frequency devices because of the splendid dielectric properties of these particles.

Corresponding Author's Email: noorulhudakhan@gmail.com

1.   Introduction

Spinel ferrites occupy polycrystalline nature. The immense significance of spinel ferrites is due to its extrinsic applications in various electronic fields. These ferrites are preferred on other materials because of its certain features like high electrical resistivity, high permeability and saturation magnetization in the radio frequency (Aslam et al., 2019). The AB_2O_4 crystal structure of spinel ferrites provides them the best magnetic properties (Peelamedu, Grimes, Agrawal, Roy, & Yadoji, 2003). The huge dialectic and electrical

characteristics of spinal ferrites depends on its chemical composition and method of its preparation (Farid et al., 2017). The significance of multi-ferroic materials is due to their ferromagnetic, ferroelectric and Ferro elastic characteristics. When the stress, magnetic field and electric field is applied on ferrites, the deformation polarization and change in spontaneous magnetization occurs respectively. The applications of these materials are in sensing, storage and spintronic devices is due to the phenomena of mutual coupling (Sheikh et al., 2019). Annealing and composition are used to control the dialectic parameters like dialectic constant, tangent loss, AC conductivity and impedance (Al-Hilli, Li, & Kassim, 2012; Nambikkattu, Kaleekkal, & Jacob, 2020). The attention towards cobalt ferrites is given because of their tremendous uses in high electromagnetic, industrial and biomedical applications. These ferrites occupy high chemical stability (Bilecka, Kubli, Amstad, & Niederberger, 2011; Franco Jr & e Silva, 2010). The reduction in saturation magnetization occurs due to the week interaction of sub lattices and decrease in magnetic moments, this is because of the ionic radii of Ce^{3+}(1.03A°) ions are larger than the Fe^{3+}(0.64A°) ions (Elayakumar et al., 2019). Structural parameters like lattice constants and crystallite size reduces. This reduction occurs because of Ce^{3+} doping which has the capability to impede the grain growth (Sobhani-Nasab, Ziarati, Rahimi-Nasrabadi, Ganjali, & Badiei, 2017). When the rare earth ions are doped to spinel structure, the interaction between Ce^{3+} and Fe^{3+} occurs with 3d-4f electron coupling. This coupling reduces the magnetic exchange interaction between A and B site which ultimately causes the small variation in magnetization due to antiferromagnetism. Interaction between the couplings of Fe^{3+}-O^{2-}-Ce^{3+} is very weak. The decrease in the saturation magnetization increases the cerium constant which makes the sample suitable for technical applications (Sagayaraj, Aravazhi, & Chandrasekaran, 2019). The details study of dielectric and impedance properties of cerium ferrites is done which were prepared by co- precipitation method.

2.   Materials and Method
2.1.   Fabrication of $Ni_{0.5}Co_{0.5}Ce_xFe_{2-x}O_4$ (x = 0.0, 0.05, 0.1, 0.15, 0.2)

Nano crystalline spinal ferrites with formula $Ni_{0.5}Co_{0.5}Ce_xFe_{2-x}O_4$ where (x = 0.0, 0.05, 0.1, 0.15, 0.2) were prepared through co- precipitation method. The chemicals used for this composition are Nickle Nitrate-6-Hydrat (Ni $(NO_3)_2.6H_2O$) M.W=290.81, made by RIEDEL-DE HEAN-A6 SEELZE-HANNOVER ,Cobalt (II) Nitrate Hexa-Hydrate (Co $(NO_3)_2.6H_2O$) M.W= 291.03 made by sigma-Aldrich, Cerium (III) Nitrate Hexa-Hydrate ($CeN_3O_9.6H_2O$) M.W= 434.2, made by Aldrich, Ferric (III) Nitrate Nano-Hydrate (Fe $(No_3)_3.9H_2O$) M.W= 404, made by GPR. Table 1 represents the various concentrations of materials used.

Table 1
Concentration of materials used

Sample no	Ni (0.4M)	Co (0.4M)	Ce (0.8M)	Fe (0.8M)
1	26mL	26mL	0.0mL	52mL
2	26mL	26mL	1.25mL	50.75 mL
3	26mL	26mL	2.5mL	49.5mL
4	26mL	26mL	3.75mL	48.25mL
5	26mL	26mL	5mL	47mL
Volume Required	130mL	130mL	12.5mL	247.5mL
Total volume	130mL	130mL	14mL	260mL

The steps followed for this experimental work are preparation of solution, stirring of solution, drying of sample, sample's grinding, annealing and pelleting. For the preparation of sample distilled water was used. Magnetic hot plate was used for stirring and mixing of all the solution of required quantities at 50° c. The PH values of all the solutions were maintain through ammonia solution. In further 5 hours the stirring of solution was done. The PH of the samples were reduce to 7 by the several times washing of precipitates. Sample's water was evaporated at 80°C in electrical oven. Muffle furnace was used to anneal the sample at 800°C for 6 hours. All The samples were grinded into powder form for the characterization purpose (Gilani et al., 2015). XRD advance diffractometer were used to examine the XRD patterns of all the compositions of $Ni_{0.5}Co_{0.5}Ce_xFe_{2-x}O_4$**.** Fourier transform infrared spectroscopy was done to investigate the chemical changes. In the frequency range

of 1-3 GHz, inspection of dielectric impedance and modulus spectroscopy was carried out at room temperature.

3. Results and Discussion
3.1. X-ray Diffraction Analysis

The structure of fabricated ferrites $Ni_{0.5}Co_{0.5}Ce_xFe_{2-x}O_4$ where (x = 0.0, 0.05, 0.1, 0.15, 0.2) and their pattern were analyzed through XRD. The Features of observed sample are given in figure 1.
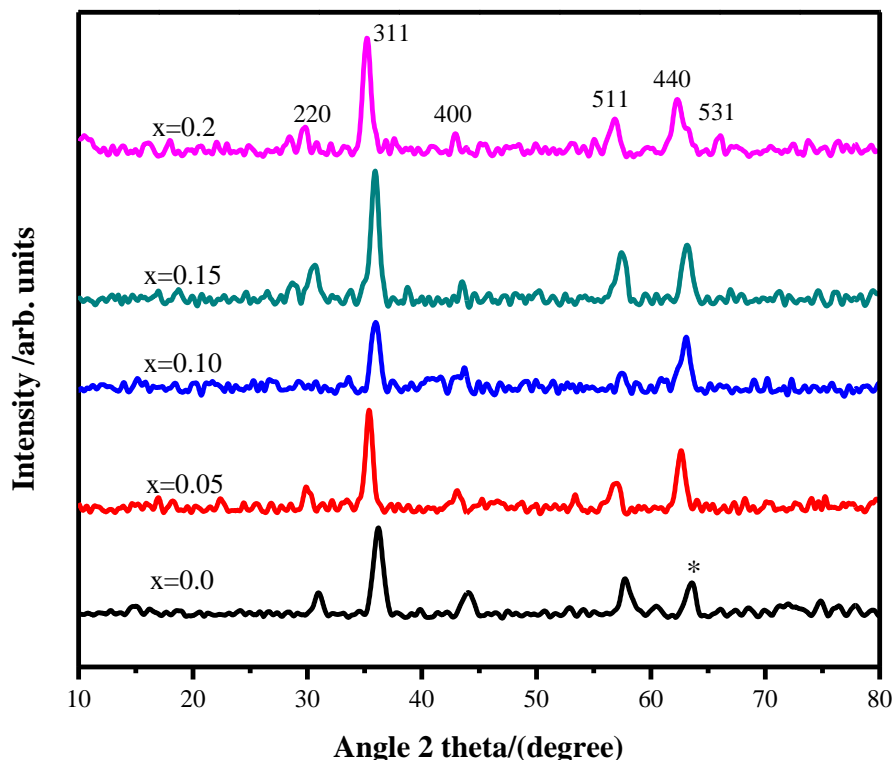

Figure 1: XRD Analysis of $Ni_{0.5}Co_{0.5}Ce_xFe_{2-x}O_4$ (x=0.0, 0.05, 0.1, 0.15, 0.2)

The annealing temperature of sample were 800°C. The FCC cubic spinel structure with single phase was obtain and it is confirmed by all the peaks in XRD patterns. The magnitude of crystalline phases is observed to alter with Ce^{3+} doping. The most strong peak is achieved at 2 = 35.56 for the concentration x=0.2, which is typically considered to be the ideal peak for cubic crystal formations. Other peak analyses were (220), (311), (400), (511), (440), and (440), (531). The presence of these peaks indicates that the prepared structure is an FCC spinel structure. JCPDS card number 22-1086 is also used to confirm the structure. The observations shows that all of the peaks were broad, indicating that the ferrite has been processed Nano crystalline structure. There are also some impurity peaks, one of which is 2 = 76.7, with a hkl value of (633). The insoluble cerium phase at the octahedral location may cause these secondary peaks to arise (Gilani et al., 2015). The appearance of this peak is may be due to the excessive Ce^{3+} ions at Octahedral site because as compared to host Fe^{3+}, they have larger ionic radii. To find the actual crystallized size Debye Scherer's formula was used (Al-Hilli et al., 2012).

D = 0.9 λ / β cosθ   (1)

The crystalline size is indicated by "D", the wave length of x-rays is lambda (1.54A°). The diffraction angle is "θ" and 'β" is for full width at half maximum. The crystalline size was observed to be 8-11 nanometer. Crystalline sizes and lattice constants of prepared samples are given in figure 2.
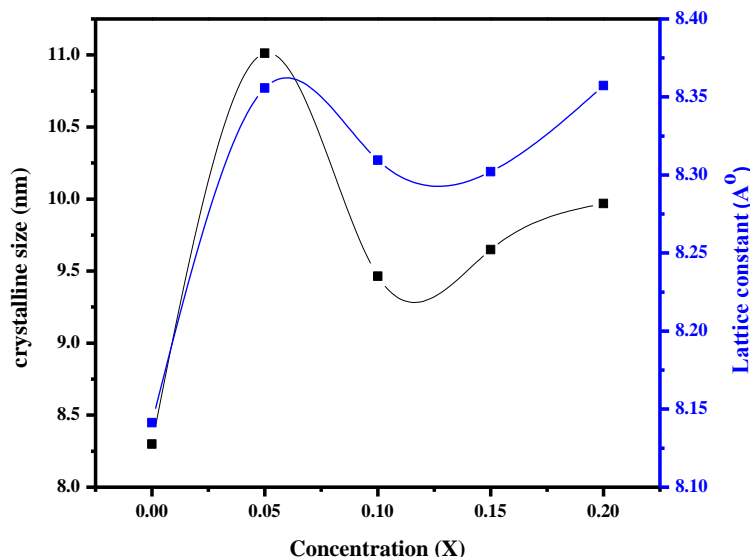
Figure 2: Crystalline size and lattice constant as a function of concentration of $Ni_{0.5}Co_{0.5}Ce_xFe_{2-x}O_4$ (x=0.0, 0.05, 0.1, 0.15, 0.2)

It is investigated that Crystalline sizes first increases then decreases with doping concentration. This inhomogeneous behavior is due to interchanging of larger ionic radii with smaller ionic radii of Fe^{3+}. It is analyzed that the lattice constant increases with the substitution of cerium which is calculated by Nelson Riley function and it is shown in figure 2. Due to their higher ionic radii, rare earth cations have a natural tendency to occupy the octahedral site (Junaid et al., 2016). The behavior of lattice parameter can be explain by Vegard's law. Many parameters, such as ionic radii, crystallite shape, surface structure, and long-range interactions, all play a role in lattice constant. Coulomb forces have an effect on the lattice constant, which could explain the previously reported abnormal behavior (Khan et al., 2020). The perimeter like cell volume, x-ray density, bulk density, lattice constant and crystalline sizes are given in the table 2. The table 2 shows the different parameters like crystalline size, lattice constant, unit cell volume, x ray density and bulk density.

Table 2
Various parameters of X-ray analysis

Parameter	X=0	X=0.05	X=0.1	X=0.15	X=0.2
Crystalline size (nm)	8.299	11.011	9.463	9.648	9.968
Lattice constant a (Å)	8.141	8.355	8.309	8.302	8.357
Cell volume (a^3)	539.6	583.3	573.7	572.2	583.6
X-ray density (g/cm^3)	5.773	5.435	5.624	5.737	5.720
Bulk density(g/cm^3)	2.827	3.293	3.589	3.280	3.662
Lattice strain x 10^{-3}	1.435	1.06	1.25	1.22	1.16
Micro strain x 10^{-3} (lines^{-2}/m^{-4})	4.17	3.14	3.66	3.59	3.47
Dislocation density x 10^{15}(lines/m^2)	14.51	8.24	11.16	10.74	10.06
Stacking fault	0.442	0.446	0.443	0.444	0.447

The observed most intense peaks are identified at (311). The increase in lattice constant is due to the larger ionic radii of cerium as compared to host cations of Fe^{3+} (Junaid et al., 2016). The relation used to calculate the X-ray density is

X-ray density = $8M / Na^3$ (2)

Molecular weight of sample is identified by "M", Avogadro's number is "N" and volume of cubic unit cell is represented by alpha3. The relation for bulk density is

Bulk density = m/v (3)

Pellet thickness is represented by "h" where "m" and "r" are mass and radius of pellet respectively.

3.2. Fourier Transform Infrared Analysis

The spinel phase of all the compositions are confirmed through FTIR. Table 3 shows the variation with Ce^{3+} concentration in vibrational bands and force factors (Aslam et al., 2019). The values of the different parameters of FTIR analysis are shown in the table 3.

Table 3
Different parameters of FTIR studies

Parameters	X=0	X=0.05	X=0.1	X=0.15	X=0.2
Molecular weight (g/mol)	235	239	243	247	251
$\upsilon 1$ (cm^{-1})	532	537	532	532	530
$\upsilon 2$ (cm^{-1})	417	418	410	418	418
K_o (dyne/cm^2) x 10^5	1.44155	1.45154	1.39938	1.45742	1.46022
K_t (dyne/cm^2) x 10^5	2.60087	2.63720	2.56791	2.62322	2.61839
R_o	0.7152	0.7689	0.7574	0.7555	0.7693
R_t	0.4426	0.4891	0.479	0.4775	0.4894

This spectroscopy also gives information about the cations distribution and chemical changes. Two main frequency bands are analyzed, one is high frequency band and other is low frequency bands. The values of these bands are around 530 cm^{-1} and 400 cm^{-1} respectively (Assar, Abosheiasha, & El Nimr, 2014; Junaid et al., 2016). The distinguishing features of spinel ferrites were thoroughly examined by these frequency bands due to the octahedral stretching bands. The vibrations in high frequency band are measured between 530 and 538 cm^{-1}, where the changes in low frequency band are measured between 410 and 418 cm^{-1}. The force constants (k_o) at octahedral side and (k_t) at tetrahedral sites are obtained by the following:

$$K_o = 0.942128\ M\ (\upsilon_2)^2\ /\ M+32 \qquad (4)$$
$$K_t = (2)^{1/2} \times K_o\ \upsilon_1/\upsilon_2 \qquad (5)$$

The tetrahedral and octahedral radii can be calculated by:

$$R_{tetra} = a\ (3)^{1/2}\ (u-0.25) - R_o \qquad (6)$$
$$R_{octa} = a\ (5/8-u) - R_o \qquad (7)$$

Where the specimen have molecular weight "M". For the fcc structure, the oxygen parameter is represented by u, and its value is 0.375. The lattice parameter is indicated by the letter "a" (Cao et al., 2018). It is observed that when cerium is doped, the strength of inter- atomic bonding increases with the increase in force factors. Figure 3 shows the FTIR spectra of $Ni_{0.5}Co_{0.5}Ce_xFe_{2-x}O_4$ (x=0.0, 0.05, 0.1, 0.15, 0.2).
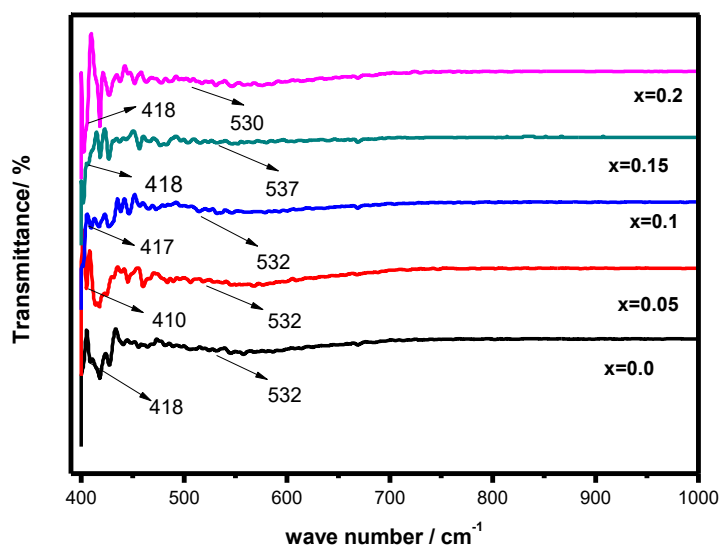

Figure 3: FTIR analysis of $Ni_{0.5}Co_{0.5}Ce_xFe_{2-x}O_4$ (x= 0.0, 0.05, 0.1, 0.15, 0.2)

3.3. Dielectric Properties

Ferrite's dielectric characteristics are critical, as we know, because of this ferrites are used in a variety of high-frequency applications. The technique of preparation, composition, and annealing time and temperature all play a role in these applications. Dielectric parameters such as dielectric loss, dielectric constant, tangent loss, real and imaginary parts of impedance, electric modulus, and AC conductivity of $Ni_{0.5}Co_{0.5}Ce_xFe_{2-x}O_4$ (x= 0.0, 0.05, 0.1, 0.15, 0.2) at room temperature were determine.

3.3.1. Dielectric Constant and Dielectric Loss

It is observed that the dielectric constant and dielectric loss disperse at high frequency. The dielectric constant increases with increased in Cerium substitution, according to the findings. In the low frequency area, it declines dramatically for all compositions with rising frequency and becomes nearly constant in the medium region up to 1.5 GHz. The phenomenon of dispersion, which occurs as a function of the applied field at lower frequencies, is linked to the reduction in dielectric constant with increasing frequency. At higher frequencies, however, similar dispersion effects are not observable. This phenomena in ferrites materials is explained by Koop's phenomenological theory and Maxwell–Wagner interfacial polarization. They proposed that at low frequencies, grain borders are more active and essential than the grains themselves due to space charge polarization, whereas at high frequencies, the opposite is true (Junaid et al., 2016).
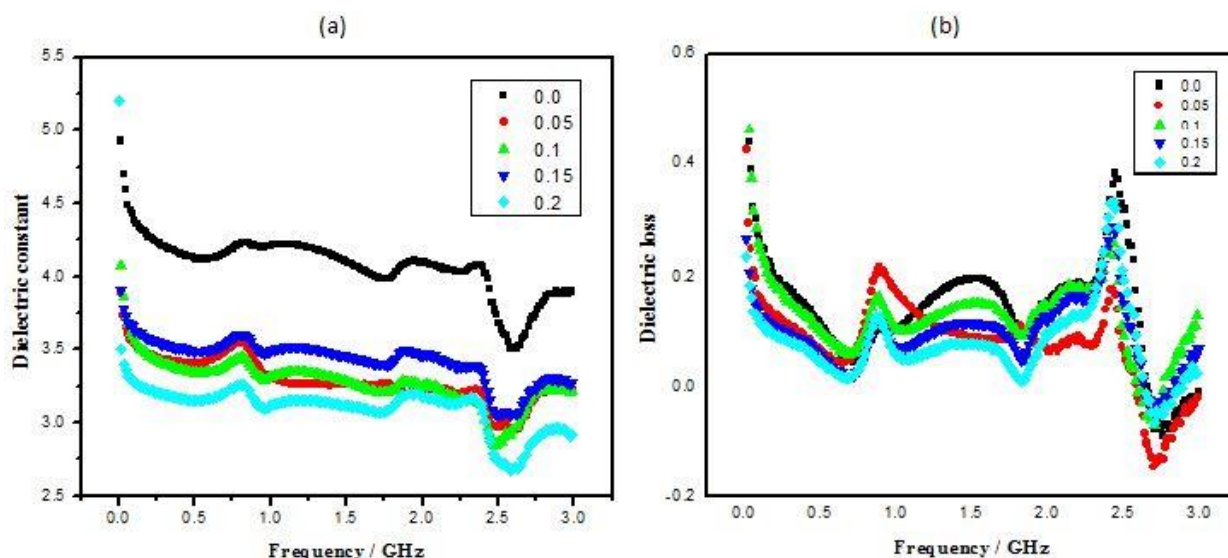

Figure 4: (a) Dielectric constant vs frequency and (b) Dielectric loss vs frequency of $Ni_{0.5}Co_{0.5}Ce_xFe_{2-x}O_4$ (x= 0.0, 0.05, 0.1, 0.15, 0.2)

These theories show that grains are more operational at high frequencies and grain borders at low frequencies are more active. At high frequencies ionic and electronic polarization occurs at grain and grain limits due to the irregular oxygen ion distribution during annealing. This irregular oxygen distribution causes low-frequency interfacial polarization. The strength of polarization decreases as the frequency increases, and the dielectric constant tends to decrease. Figure 4 (a) and (b) shows the dielectric constant and dielectric loss respectively. At the octahedral site, the electron exchange takes place between Fe^{3+} and Fe^{2+}. Electronic hopping reduces the dielectric constant because it does not follow the pattern of the applied alternating field at high frequencies (Decker, 2016). The minimum dielectric loss value of 2.6 GHz is observed.

3.3.2. Tangent Loss and AC conductivity

The observed variation in tangent loss is the same as the observed variation in the dielectric constant and the variation in the dielectric loss. In low frequency, the tangent loss is high as hopping electrons are parallel to field's frequency, but at high frequency hopping

electrons, refuse to obey the applied frequency which causes the tangent loss to decrease after some critical frequencies (Sheikh et al., 2019). Figure 5 clearly shows that tangent loss is considerable at low frequencies and steadily diminishes as frequency increases, as predicted by Koops' phenomenological theory. The reduced tangent loss of Nano ferrites is critical in a variety of applications. AC conductivity is the most important characteristic in dielectric material. At room temperature, the AC conductivity of a synthesized ferrite sample with composition $Ni_{0.5}$ $CO_{0.5}$ Ce_x Fe_{2-x} O_4 (x=0.0, 0.05, 0.1, 0.15, and 0.2) is observed in the range of 1 to 3 GHz frequency. The AC conductivity has the formula:

$$\sigma_{ac} = t/A(Z')/Z'^2 + Z''^2 \tag{8}$$

Where "t" represents the thickness of the pellet, A represents the area, and Z' and Z" represent the real and imaginary impedance, respectively. The ratio of ε′ and ε′′ with loss tangent (tan Ś) is described by:

$$Tan\ \delta =\ \varepsilon''/\ \varepsilon' \tag{9}$$

The graph below depicts the conductivity of alternating current (Sheikh et al., 2019). The figure shows that all samples show the same behavior at low frequency (increasing trend). The Maxwell Wagner heterogeneous model can also be used to explain the frequency dependence of AC conductivity. The structure of dielectric materials, according to this hypothesis, is made up of two layers. The first layer is made up of well-conducting grain, whereas the second layer is made up of grain boundaries that are very resistant. Highly resistive grain boundaries become more active at low frequencies, preventing electron transfer between Fe^{3+} and Fe^{2+} cations. As a result, the ac conductivity decreases. Conducting grains becomes active at increasing frequencies of an alternating field, and electron hoping between Fe^{3+} and Fe^{2+} cations increases. AC conductivity rises in lockstep with hopping (Kamran & Anis-ur-Rehman, 2020). Different parameters like dielectric constant, dielectric loss and tangent loss are given in the table 4.

Table 4
Different dielectric parameters of $Ni_{0.5}Co_{0.5}Ce_xFe_{2-x}O_4$ (x= 0.0, 0.05, 0.1, 0.15, 0.2)

Parameters	Frequency	x=0.0	x=0.05	x=0.10	x=0.15	x=0.20
	1MHz	10.72	7.6	10.11	5.57	5.2
Dielectric	1GHz	4.21	3.3	3.31	3.49	3.11
constant	2.5GHz	3.68	2.98	2.86	3.05	2.73
	3GHz	3.9	3.21	3.2	3.24	2.9
	1MHz	5.078	3.75	5.37	2.21	1.78
Dielectric loss	1GHz	0.098	0.17	0.1	0.06	0.05
	2.5GHz	0.318	0.06	0.087	0.15	0.19
	3GHz	-0.011	-0.008	0.14	0.07	0.032
	1MHz	0.473	0.49	0.53	0.39	0.34
Tangent loss	1GHz	0.023	0.05	0.03	0.02	0.017
	2.5GHz	0.086	0.02	0.03	0.05	0.071
	3GHz	-0.003	-0.0024	0.043	0.02	0.011
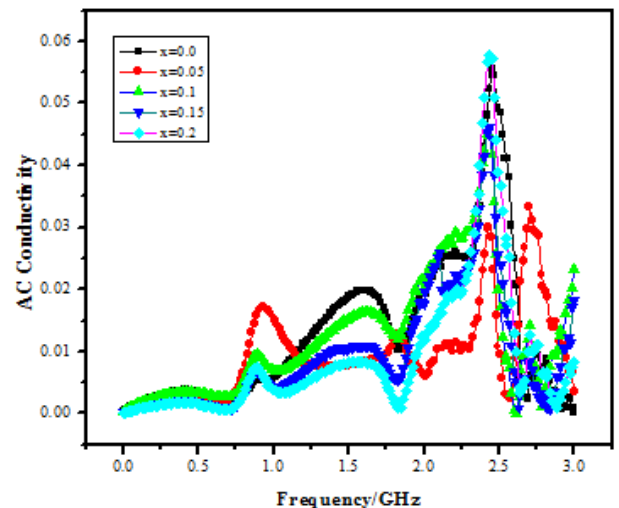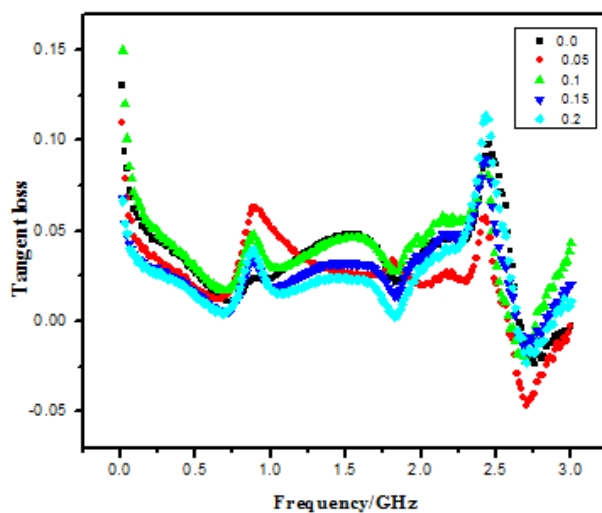
Figure 5: (a) Tangent loss vs frequency and (b) AC conductivity vs frequency of Ni$_{0.5}$Co$_{0.5}$Ce$_x$Fe$_{2-x}$O$_4$ (x= 0.0, 0.05, 0.1, 0.15, 0.2)

3.3.3.Real and Imaginary Impedance

Impedance plays a vital role in the dielectric properties of the material. Figure 6 (a) and (b) represents the real and imaginary impedance vs. log f.
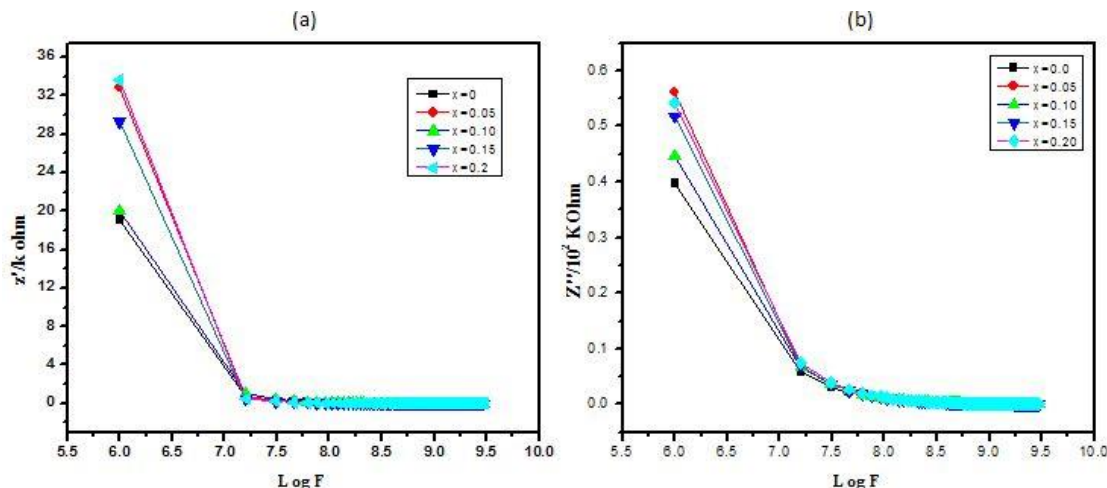

Figure 6: (a) Log f vs real impedance and (b) Log f vs imaginary impedance of Ni$_{0.5}$Co$_{0.5}$Ce$_x$Fe$_{2-x}$O$_4$ (x= 0.0, 0.05, 0.1, 0.15, 0.2)

The frequency applied influenced the real and imaginary impedance strictly. Real and imaginary impedance parts can be calculated using formulas

$$Z^{/} = R = /Z/ \cos \theta_z \qquad (10)$$
$$Z^{//} = X = /Z/ \sin\theta_z \qquad (11)$$

The research reveals that applied frequency has an inverse relationship with real and imaginary impedance, implying that as frequency rises, imaginary and real impedance fall. All sample impedance curves merge at higher frequency. The constant higher frequency impedance is attributed to release of space charges. These space charges are formed as a result of the concentration differential as well as the inhomogeneity of the applied field. The concentration difference and inhomogeneity of the applied field combines the spatial charges at the grain limits. The reduction in the real and imaginary impedance manifests improved conductivity if the frequency applied is increased (Parveen et al., 2019).

3.3.5 Real and Imaginary Modulus

The real and imaginary modulus qualities can be used to explain the purpose of grains and grains boundaries on a certain frequency range.
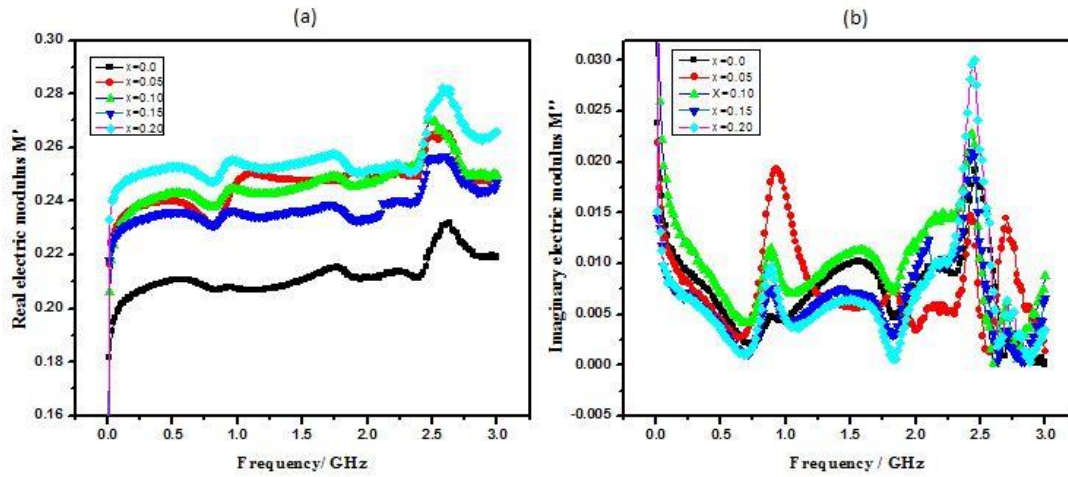
Figure 7: (a) Real modulus vs frequency and (b) Imaginary modulus vs frequency of $Ni_{0.5}Co_{0.5}Ce_xFe_{2-x}O_4$ (x= 0.0, 0.05, 0.1, 0.15, 0.2)

Different values of dielectric parameters like AC conductivity, Z', Z'', M' and M'' are given below in table 5.

Table 5
Various parameters of dielectric of $Ni_{0.5}Co_{0.5}Ce_xFe_{2-x}O_4$ (x= 0.0, 0.05, 0.1, 0.15, 0.2)

	Frequency	Concentrations				
		x=0.0	x=0.05	x=0.1	x=0.15	x=0.2
AC conductivity	1 MHz	2.818×10^{-4}	2.232×10^{-4}	2.1402×10^{4}	1.484×10^{-4}	1.305×10^{-4}
	1 GHz	5.858×10^{-3}	1.502×10^{-2}	6.842×10^{-3}	4.231×10^{-3}	3.654×10^{-3}
	2.5 GHz	4.856×10^{-2}	9.59×10^{-3}	1.7228×10^{-2}	2.97×10^{-2}	3.680×10^{-2}
	3 GHz	1.621×10^{-4}	3.53×10^{-3}	2.3387×10^{-2}	1.8153×10^{-2}	8.358×10^{-3}
Z'/Ohm	1 MHz	1.912×10^{4}	3.292×10^{4}	2.0047×10^{4}	2.9345×10^{4}	3.6111×10^{4}
	1 GHz	2.306	8.454	3.74	2.153	2.166
	2.5 GHz	3.607	0.983	1.852	2.324	4.162
	3 GHz	8.02×10^{-3}	0.2252	1.5024	1.1374	0.6073
Z''/Ohm	1 MHz	3.9724×10^{4}	5.605×10^{4}	4.4593×10^{4}	6.9315×10^{4}	7.9029×10^{4}
	1 GHz	1.061×10^{2}	1.267×10^{2}	1.2508×10^{2}	1.2073×10^{2}	1.3024×10^{2}
	2.5 GHz	4.5985×10^{1}	5.421	5.5455×10^{1}	5.2653×10^{1}	5.6770×10^{1}
	3 GHz	3.7641×10^{1}	4.275	4.2869×10^{1}	4.2349×10^{1}	4.5617×10^{1}
M'	1 MHz	7.7161×10^{-2}	1.089×10^{-1}	8.6618×10^{-2}	1.3463×10^{-1}	1.535×10^{-1}
	1 GHz	2.073×10^{-1}	2.475×10^{-1}	2.4432×10^{-1}	2.3584×10^{-1}	2.545×10^{-1}
	2.5 GHz	2.2376×10^{-1}	2.638×10^{-1}	2.6984×10^{-1}	2.5621×10^{-1}	2.763×10^{-1}
	3 GHz	2.1934×10^{-1}	2.49×10^{-1}	2.4980×10^{-1}	2.477×10^{-1}	2.658×10^{-1}
M''	1 MHz	3.7145×10^{-2}	6.395×10^{-2}	3.8939×10^{-2}	5.7001×10^{-2}	6.529×10^{-2}
	1 GHz	4.503×10^{-3}	1.652×10^{-2}	7.306×10^{-3}	4.421×10^{-3}	4.232×10^{-3}
	2.5 GHz	1.7552×10^{-2}	4.79×10^{-3}	9.01×10^{-3}	1.131×10^{-2}	2.025×10^{-2}
	3 GHz	4.67×10^{-5}	1.312×10^{-3}	8.755×10^{-3}	6.628×10^{-3}	3.538×10^{-3}

The following formulas can be used to calculate the real and imaginary modulus.

$$M' = \epsilon' / (\epsilon'^2 + \epsilon''^2) \tag{12}$$
$$M'' = \epsilon'' / (\epsilon'^2 + \epsilon''^2) \tag{13}$$

Figure 7 (a) and (b) shows that the frequency has a direct relationship with the real and imaginary modulus. The real and imaginary modulus have smaller values at low frequencies, and the modulus increases as the frequency rises. The greatest modulus values are found at 3 GHz frequency (Rodrigues & McPhaden, 2014). The M' and M'' have tiny values and little fluctuation at low frequencies, as shown in the figure. Two opposed peaks (trough for real impedance and crest for imaginary impedance) are found due to relaxation phenomena (frequency dependent variation in conductivity). Variations in dopant concentration cause a shift in the peak frequency (Khan et al., 2020). The different values of M' and M'' for the frequency ranges of 1MHz, 2MHz, 2.5 GHz, and 3GHz were analyzed, and it can be seen that the AC conductivity, real parts of modulus (M'), imaginary parts of modulus (M'), real parts of impedance (Z'), and imaginary parts of impedance (Z') vary in a inhomogeneous manner.

4. Conclusions

The Nano-Crystalline ferrite synthesized with the general formula $Ni_{0.5}Co_{0.5}Ce_xFe_{2-x}O_4$ (x=0.0, 0.05, 0.15, 0.2). The Ce^{3+} substitution clearly affects the structural and electrical characteristics. The crystalline dimensions of Nano ferrites are calculated using the Debye Scherer formula and are between 8 nm and 11 nm. It was discovered that crystalline size does not changes uniformly with doping. The calculations demonstrate that grain sizes correlate with XRD data, confirming the crystalline size of the manufactured samples. The observations show that the extreme peaks were identified at 2θ = 35 with (311) hkl utility, which are the optimum peaks for spinel ferrite Nano particles. There is a similarity of indexed peaks (220) (311) (400) (531) with a spinel structure. The lattice constant is observed as a growing trend. The increase in doping concentration also increases cell volume. The systematic variations and chemical effects of Fourier transform Infrared Spectroscopy (FTIR) are identified in octahedral and tetrahedral sites, there is a constant force range of 1.441×10^5 to 1.460×10^5 and 2.60×10^5 to 2.618×10^5, respectively. The range of the octahedral radii is between 0.715 and 0.769 and the tetrahedral radii between 0.442 and 0.489. Dielectric properties are observed in the 1 MHz to 3 GHz frequency range. Dielectric constant, dielectric loss and tangent loss is seen in the dielectric study to decrease in trend. The impedance of the composed spinal ferrite is strengthened by increasing the doping concentration of rare earth ion. This is owing to the fact that as frequency rises, impedance decreases. Because of the hopping mechanism, AC conductivity spectra show continuous behavior at low frequencies but dispersion at high frequencies. The study of the real and imagination modulus shows that the effect of low-frequency grain boundaries is high. The excellent electrical properties of ferrites ensure that these materials are used for pharmacological delivery, cancer treatment, high frequency applications, microwave applications, storage and semiconductor devices.

Acknowledgement

References

Al-Hilli, M. F., Li, S., & Kassim, K. S. (2012). Structural analysis, magnetic and electrical properties of samarium substituted lithium–nickel mixed ferrites. *Journal of Magnetism and Magnetic Materials, 324*(5), 873-879.

Aslam, S., Shifa, M. S., Gilani, Z. A., Usmani, M. N., Rehman, J. U., Khan, M. A., . . . Khalid, M. (2019). Structural, optical and magnetic elucidation of co-doping of Nd3+ and Pr3+ on lithium nanoferrite and its technological application. *Results in Physics, 12*, 1334-1339.

Assar, S., Abosheiasha, H., & El Nimr, M. (2014). Study of the dielectric behavior of Co–Ni–Li nanoferrites. *Journal of Magnetism and Magnetic Materials, 350*, 12-18.

Bilecka, I., Kubli, M., Amstad, E., & Niederberger, M. (2011). Simultaneous formation of ferrite nanocrystals and deposition of thin films via a microwave-assisted nonaqueous sol–gel process. *Journal of sol-gel science and technology, 57*(3), 313-322.

Cao, D., Pan, L., Li, J., Cheng, X., Zhao, Z., Xu, J., . . . Wang, J. (2018). Investigation on the structures and magnetic properties of carbon or nitrogen doped cobalt ferrite nanoparticles. *Scientific reports, 8*(1), 1-9.

Decker, F. (2016). The "Alternative for Germany": Factors behind its emergence and profile of a new right-wing populist party. *German Politics and Society, 34*(2), 1-16.

Elayakumar, K., Dinesh, A., Manikandan, A., Palanivelu, M., Kavitha, G., Prakash, S., . . . Baykal, A. (2019). Structural, morphological, enhanced magnetic properties and antibacterial bio-medical activity of rare earth element (REE) cerium (Ce3+) doped CoFe2O4 nanoparticles. *Journal of Magnetism and Magnetic Materials, 476*, 157-165.

Farid, H. M. T., Ahmad, I., Ali, I., Ramay, S. M., Mahmood, A., & Murtaza, G. (2017). Dielectric and impedance study of praseodymium substituted Mg-based spinel ferrites. *Journal of Magnetism and Magnetic Materials, 434*, 143-150.

Franco Jr, A., & e Silva, F. (2010). High temperature magnetic properties of cobalt ferrite nanoparticles. *Applied Physics Letters, 96*(17), 172505.

Gilani, Z. A., Warsi, M. F., Khan, M. A., Shakir, I., Shahid, M., & Anjum, M. N. (2015). Impacts of neodymium on structural, spectral and dielectric properties of LiNi0. 5Fe2O4 nanocrystalline ferrites fabricated via micro-emulsion technique. *Physica E: Low-dimensional Systems and Nanostructures, 73*, 169-174.

Junaid, M., Khan, M. A., Iqbal, F., Murtaza, G., Akhtar, M. N., Ahmad, M., . . . Warsi, M. F. (2016). Structural, spectral, dielectric and magnetic properties of Tb–Dy doped Li-Ni nano-ferrites synthesized via micro-emulsion route. *Journal of Magnetism and Magnetic Materials, 419*, 338-344.

Kamran, M., & Anis-ur-Rehman, M. (2020). Enhanced transport properties in Ce doped cobalt ferrites nanoparticles for resistive RAM applications. *Journal of Alloys and Compounds, 822*, 153583.

Khan, J. K., Khalid, M., Chandio, A. D., Shahzadi, K., Uddin, Z., Mustafa, G., . . . Gilani, Z. A. (2020). Properties of Al 3+ substituted nickel ferrite (NiAl x Fe 2-x O 4) nanoparticles synthesised using wet sol-gel auto-combustion. *Journal of Sol-Gel Science and Technology*, 1-12.

Nambikkattu, J., Kaleekkal, N. J., & Jacob, J. P. (2020). Metal ferrite incorporated polysulfone thin-film nanocomposite membranes for wastewater treatment. *Environmental Science and Pollution Research*, 1-13.

Parveen, A., Khalid, M., Gilani, Z. A., Aslam, S., Saleem, M., Shaikh, F. A., & Rehman, J. (2019). Dielectric, impedance and modulus spectroscopic studies of Co 0.3 Cd 0.7 Zn 1.5 x Fe 2− x O 4 nanoparticles. *Applied Physics A, 125*(10), 1-11.

Peelamedu, R., Grimes, C., Agrawal, D., Roy, R., & Yadoji, P. (2003). Ultralow dielectric constant nickel–zinc ferrites using microwave sintering. *Journal of materials research, 18*(10), 2292-2295.

Rodrigues, R. R., & McPhaden, M. J. (2014). Why did the 2011–2012 La Niña cause a severe drought in the Brazilian Northeast? *Geophysical Research Letters, 41*(3), 1012-1018.

Sagayaraj, R., Aravazhi, S., & Chandrasekaran, G. (2019). Effect of Zinc Content on Structural, Functional, Morphological, Resonance, Thermal and Magnetic Properties of Co 1− x Zn x Fe 2 O 4/PVP Nanocomposites. *Journal of Inorganic and Organometallic Polymers and Materials, 29*(6), 2252-2261.

Sheikh, F. A., Khalid, M., Shifa, M. S., Aslam, S., Perveen, A., ur Rehman, J., . . . Gilani, Z. A. (2019). Effects of bismuth on structural and dielectric properties of cobalt-cadmium spinel ferrites fabricated via micro-emulsion route. *Chinese Physics B, 28*(8), 088701.

Sobhani-Nasab, A., Ziarati, A., Rahimi-Nasrabadi, M., Ganjali, M. R., & Badiei, A. (2017). Five-component domino synthesis of tetrahydropyridines using hexagonal PbCr x Fe 12− x O 19 as efficient magnetic nanocatalyst. *Research on Chemical Intermediates, 43*(11), 6155-6165.